This is a preprint, the final version is subject to change, of the American Mineralogist (MSA)
Cite as Authors (Year) Title. American Mineralogist, in press.
DOI: https://doi.org/10.2138/am-2020-7106

Revision 1

Dissolution of Poorly Soluble Uranyl Phosphate Phases in the Metaautunite Subgroup Under Uranyl Peroxide Cage Cluster Forming Conditions

Haylie L. Lobeck,[1] Enrica Balboni,[1, †] Connor J. Parker, [1, §] Tsuyoshi A. Kohlgruber,[1] Mengyu Xu,[1] Sara Boukdad,[1] Henry M. Ridder,[2] Hrafn Traustason,[3] Jordan K. Isner,[2] Ewa A. Dzik, [1] and Peter C. Burns [1,3]*

[1] Department of Civil and Environmental Engineering and Earth Sciences, University of Notre Dame, Notre Dame, IN 46556, USA

[2] Department of Chemical and Biomolecular Engineering, University of Notre Dame, Notre Dame, IN 46556, USA

[3] Department of Chemistry and Biochemistry, University of Notre Dame, Notre Dame, IN 46556, USA

† Present Address: Glenn T. Seaborg Institute, Physical & Life Sciences Directorate, Lawrence Livermore National Laboratory, Livermore, CA 94550, USA

§ Present Address: Environmental Engineering and Earth Sciences, Clemson University, Anderson, SC 29625, USA

* Corresponding author: Peter C. Burns email: pburns@nd.edu

This is a preprint, the final version is subject to change, of the American Mineralogist (MSA)
Cite as Authors (Year) Title. American Mineralogist, in press.
DOI: https://doi.org/10.2138/am-2020-7106

Abstract

Uranyl phosphate minerals are widespread in uranium deposits and normally exhibit very low solubility in aqueous systems. Uranyl phosphates of the autunite group and metaautunite subgroup impact the mobility of uranium in the environment and have inspired groundwater remediation strategies that emphasize their low solubility. The importance of soluble uranium-bearing macroanions, including nanoscale uranyl peroxide cage clusters, is largely unexplored relative to solubilization of normally low solubility uranium minerals. Eight synthetic analogues of metaautunite subgroup minerals have been prepared and placed in various alkaline aqueous solutions containing hydrogen peroxide and tetraethylammonium hydroxide. Each uranyl phosphate studied has a topologically identical anionic sheet of uranyl square bipyramids and phosphate tetrahedra combined with various cations (Li^+, Na^+, K^+, Rb^+, Cs^+, Mg^{2+}, Ca^{2+}, Ba^{2+}) and water in the interlayer. Uranyl peroxides formed under many of the experimental conditions examined including solid studtite $[(UO_2)(O_2)(H_2O)_2](H_2O)_2$ and soluble uranyl peroxide cage clusters containing as many as 28 uranyl ions. Uranyl phosphate solids in contact with solutions in which uranyl peroxide cage clusters formed dissolved extensively or completely. The greatest dissolution of uranyl phosphates occurred in systems that contained cations with larger hydrated radii, Li^+ and Na^+. The details of the uranium speciation in solution depended on the pH and counter cations provided from the interlayers of the uranyl phosphate solids.

Keywords

Metaautunite, dissolution, uranium, studtite, uranyl peroxide nanoclusters, peroxide, uranyl phosphate

Introduction

Uranyl phosphates, particularly of the autunite group and metaautunite subgroup, are widespread constituents in oxidized portions of uranium deposits, and are important relative to the environmental transport of uranium and the nuclear fuel cycle due to their low aqueous solubility (Astilleros et al. 2013; Buck et al. 1996; Dzik et al. 2017a; Gudavalli et al. 2018; Locock et al. 2004a, 2004b; Suzuki et al. 2005; Wellman et al. 2006a;). In addition to their occurrence in natural uranium deposits (Krivovichev and Plášil 2013; Murakami et al. 1997) and contaminated sites (such as Hanford, WA) (Perdrial et al. 2018; Reynolds et al. 2018; Singer et al. 2009), formation of uranyl phosphates has been proposed as a remediation strategy for removal of soluble uranium from water (Fanizza et al. 2013; Fuller et al. 2002; Lammers et al. 2017; Mehta et al. 2014, 2015; Munasinghe et al. 2015; Wellman et al. 2006b, 2007a, 2008; Raicevic et al. 2006). Members of the autunite group have composition $A^{n+}[(UO_2)(TO_4)](H_2O)_m$ where A^{n+} is a mono-, di-, or trivalent cation, T is P or As, and m is the number of water molecules. The structural unit is $[(UO_2)(TO_4)]^-$ sheets consisting of uranyl square bipyramids that share equatorial vertices with four different TO_4 tetrahedra. Cations and water are in the weakly bonded interstitial complex located between the sheets (Figure 1) (Burns 2005) and provide linkages between the sheets (Locock et al. 2004a; Locock 2007). The thermodynamic properties (Dzik et al. 2017a, 2017b; Gorman-Lewis et al. 2009), aqueous solubility (Gorman-Lewis et al. 2009; VanHaverbeke et al. 1996), and dissolution behaviors in acidic conditions (Wellman et al. 2007b) of members in the metaautunite subgroup have been studied, although their behavior in alkaline systems containing hydrogen peroxide is unknown.

Studtite, $[(UO_2)(O_2)(H_2O)_2](H_2O)_2$, is a poorly soluble uranyl peroxide mineral comprised of infinite chains of uranyl hexagonal bipyramids linked together by peroxide bridges

(Burns and Hughes 2003). It readily forms as an alteration product when uranium material, ranging from UO_2 to uranyl oxide hydrates to uranyl silicates, comes in contact with solutions containing hydrogen peroxide in acidic and neutral environments (Abrefah et al. 1998; Armstrong et al. 2012; Burns and Hughes 2003, Burns et al. 2012; Clarens et al. 2005; Forbes et al. 2011; Hanson et al. 2005; Magnin et al. 2015). Studtite is commonly used in the nuclear fuel cycle to control the solubility of uranium in water, and modern yellowcake often contains substantial studtite (Mallon et al. 2012; Odoh et al. 2016). Recent studies have shown that studtite transforms to soluble uranyl peroxide nanoscale cage clusters in alkaline aqueous systems with and without the presence of additional hydrogen peroxide (Lobeck et al. 2019a).

Uranyl peroxide clusters are hollow anionic cage-like nanoscale structures composed of 16 to 124 uranyl ions bridged by peroxide and hydroxyl (or other ligands) (Burns 2011; Burns and Nyman 2018; Qiu and Burns 2013). Uranyl peroxide clusters persist in aqueous systems and can support very high concentrations of uranium (up to 42 wt. % U) in solution (Hickam et al. 2018; Peruski et al. 2016). Introducing normally poorly soluble uranium materials such as studtite, UO_2, or UN into alkaline aqueous solutions containing hydrogen peroxide can result in the formation of uranyl peroxide nanoclusters such as U_{20} $[(UO_2)_{20}(O_2)_{30}]^{20-}$, U_{24} $[(UO_2)_{24}(O_2)_{24}(OH)_{24}]^{24-}$, U_{28} $[(UO_2)_{28}(O_2)_{42}]^{28-}$, U_{30} $[(UO_2)_{30}(O_2)_{36}(OH)_{22}]^{34-}$, and U_{32} $[(UO_2)_{32}(O_2)_{32}(OH)_{32}]^{32-}$ (Figure 2) (Burns and Nyman 2018; Falaise and Nyman 2016; Hickam et al. 2018, 2019; Lobeck et al. 2019a; Unruh et al. 2010). The type and quantity of counter cation in the system impacts nanocluster formation and dissolution of the poorly soluble uranium materials (Burns and Nyman 2018; Falaise and Nyman 2016; Hickam et al. 2018; Lobeck et al. 2019a).

In the current study, conditions are delineated under which uranyl peroxide nanoclusters form due to alteration of uranyl phosphate minerals, as well as the importance of the counter cations in these systems. Eight synthetic analogs of metaautunite subgroup minerals were studied: $Li[(UO_2)(PO_4)](H_2O)_4$ (designated *LiUP*), $Na[(UO_2)(PO_4)](H_2O)_3$ (metanatroautunite, *NaUP*), $K[(UO_2)(PO_4)](H_2O)_3$ (metaankoleite, *KUP*), $Rb[(UO_2)(PO_4)](H_2O)_3$ (*RbUP*), $Cs[(UO_2)(PO_4)](H_2O)_{2.5}$ (*CsUP*), $Mg[(UO_2)_2(PO_4)_2](H_2O)_{10}$ (saléeite, *MgUP*), $Ca[(UO_2)_2(PO_4)_2](H_2O)_6$ (metaautunite, *CaUP*), and Ba[(UO2)2(PO4)2](H2O)6 (metauranocircite, *BaUP*) .

Experimental Section

Synthesis of Uranyl Phosphate Phases

Synthetic analogs of uranyl phosphate minerals were prepared by slow mixing of reactants by liquid diffusion, following a method first established by Fernelius in 1934 and recently adapted for uranyl compounds (Dzik et al. 2017a; Fernelius and Detling 1934). Two clean 2-mL glass vials were arranged within a 100-mL glass beaker isolated from the walls and each other (Figure 3). Each vial was filled with either 1.5 mL of a 0.5 M $(UO_2)(NO_3)_2$ aqueous solution or a 0.5 M H_3PO_4 aqueous solution. A dilute cation-bearing nitrate barrier solution (0.01 M $LiNO_3$, $NaNO_3$, KNO_3, $RbNO_3$, $CsNO_3$, $Mg(NO_3)_2$, $Ca(NO_3)_2$, or $Ba(NO_3)_2$) was slowly added to fill the remaining volume within the small vials and the 100-mL beaker until both vials were fully submerged (~80 mL). The 100 mL beaker was then covered by Parafilm and left on the bench top for nine to fifteen days. Over that time, the uranyl nitrate and phosphoric acid solutions slowly diffused through the cation barrier solution and co-mingled to produce crystals of the targeted phase, typically on the rim of the 2-mL vial that contained the uranyl nitrate

114 solution. Crystals were recovered by vacuum filtration and rinsed with ultrapure (18 MΩ) water.
115 Once dry, the crystals were ground to a powder with a mortar and pestle and characterized with
116 powder X-ray diffraction for phase confirmation and to determine purity (Table 1, Figures S1 –
117 S8).
118
119 **Dissolution of Uranyl Phosphate Phases**
120 To study the dissolution of the uranyl phosphate solids over a range of aqueous alkaline
121 peroxide-containing systems, 30.0 ± 0.5 mg of the powdered uranyl phosphate was combined
122 with 1.6 mL of ultrapure water containing hydrogen peroxide at concentrations of 0.01 M, 0.035
123 M, 0.10 M, 0.50 M, or 1.0 M in a 7 mL capped Teflon vial. The solutions and synthetic phases
124 were then mixed continuously (except during pH adjustment) on a rotator for seven days. The pH
125 was adjusted daily by adding tetraethylammonium hydroxide (TEAOH) to achieve one of the
126 target values of 7, 8, 9, 10, or 11. The 40% TEAOH stock solution used in these experiments was
127 shown by chemical analysis to contain a minor but detectable K^+ contaminant. Two sets of
128 control reactions were used in these experiments to characterize the behavior of the uranyl
129 phosphate phases in (A) water at pH 7 to 11 with no added peroxide and (B) hydrogen peroxide
130 solutions without the addition of base. The measured pH of control B reactions ranged from 2.4 –
131 5.1 over the range of peroxide concentrations. On day seven, each mixture was centrifuged at
132 13,000 rpm for 10 minutes and the solution was extracted from the remaining powder. The
133 powder was rinsed twice with ultrapure water to remove any remaining solution and was set to
134 dry on the benchtop. Replicate experiments at each reaction condition were performed.
135 Time resolved dissolution studies of metaautunite, *CaUP*, in 1.0 M peroxide in alkaline
136 conditions with pH greater than 10 revealed that the reactions achieved a steady state of uranium

dissolved in solution by day three (Figure S9). Each experiment within this body of work was reacted for a seven days, and solution analysis was performed within two days of harvesting to ensure consistency throughout the experimental results.

Powder X-Ray Diffraction (PXRD)

Powder X-ray diffraction (PXRD) measurements were conducted on a Bruker D8 Davinci diffractometer equipped with Cu$K\alpha$ radiation and a solid-state detector. Samples were prepared by dry mounting 10 mg of finely ground powder on a zero-background oriented quartz slide. Patterns were collected using a sample rotation speed of 15 rotations per minute, a 2θ range from 5 - 55°, a step size of 0.01° or 0.02°, and a scan rate of 0.5 or 1.0 seconds per step.

Inductively Coupled Plasma – Optical Emission Spectrometry (ICP-OES)

Samples for chemical analysis by inductively coupled plasma – optical emission spectrometry (ICP-OES) were prepared by either dissolving 10 mg solid samples in 15.8 M HNO_3 and further diluting the sample in a 5% HNO_3 matrix, or by diluting aliquots of solution in a 5% HNO_3 matrix. Elemental analyses were performed using a PerkinElmer Optima 8000 instrument with 165 – 800 nm coverage and a resolution of approximately 0.01 nm for multi-elemental analysis. Ten calibration standards were prepared with U concentrations ranging from from 0.01 to 40 ppm, and a 0.5 ppm Y internal standard was added to each sample, blank, and standard to monitor for instrumental drift.

Electrospray Ionization Mass Spectrometry (ESI-MS)

Electrospray ionization mass spectra (ESI-MS) were acquired using a Bruker microTOF-Q II high-resolution quadrupole time of flight (Q-TOF) spectrometer in negative ion mode (3700 V capillary voltage, an endplate offset of -500 V, 3.6 bar nebulizer gas, 5 L min^{-1} dry gas, 180°C dry gas temperature). Samples were diluted to a uranium concentration less than 100 ppm and were introduced into the spectrometer by direct injection at a rate of 500 μL hr^{-1}. Spectra were collected over a 500-5000 m/z range with data averaged over three minutes. Data was deconvoluted using the MaxEnt feature of the Bruker DataCompass data-analysis software.

Raman Spectroscopy

Raman spectra were collected using a Renishaw InVia Raman spectrometer equipped with a 785 nm laser and 1200-line mm^{-1} grating. Spectra of solutions were acquired with a static scan over the range of 508 – 1075 cm^{-1} using four 10-second exposures at 10% laser power. Baseline corrections were performed for the final data using the Renishaw WiRE software.

^{31}P Nuclear Magnetic Resonance Spectroscopy (^{31}P NMR)

^{31}P NMR measurements were performed for aqueous solutions using a 600 MHz Varian INOVA spectrometer (11.74 T) with a pulse length of 14.8 ms, 64 scans, and a relaxation time (d1) of 10 s.

Small angle X-ray Scattering (SAXS)

Small-angle X-ray scattering (SAXS) data was collected using a Bruker Nanostar equipped with an Incoatec Microfocus X-ray source with Cu$K\alpha$ (1.5406 Å) radiation with a point collimation system. Solutions were placed in 0.5 mm diameter quartz capillaries with 0.01 mm

wall thickness. The ends of the capillaries were sealed using Torr Seal low vapor pressure epoxy. A scattering pattern for each sample was collected for two hours without glassy carbon standard and four minutes with glassy carbon standard. Each scattering pattern was matrix background subtracted and integrated using the DIFFRAC.EVA software program. The radius of gyration was calculated by best fit to the experimental data using the Irena SAS package in the Igor Pro software (Ilavsky and Jemian 2009).

Results

Characterization of Solid Phases

Powder X-ray diffraction patterns collected for the as-synthesized uranyl phosphate compounds confirmed their identity and purity. Observed patterns are compared to expected peak positions in the Supporting Information (Figure S1 – S8).

Upon termination of dissolution experiments any remaining solid was collected for analysis. Figure 4 shows the powder X-ray diffraction patterns of solids recovered from experiments in which *LiUP* was reacted with a 0.5 M peroxide solution at various pH values (data for other reaction conditions are in Supporting Information). Studtite, $[(UO_2)(O_2)(H_2O)_2](H_2O)_2$, was the only crystalline solid phase present after *LiUP* was mixed with an aqueous solution of 0.5 M H_2O_2 for seven days without pH adjustment (the solution pH was 3). Solids recovered after reaction of *LiUP* with aqueous solutions at pH 7 to 10 and an initial H_2O_2 concentration of 0.5 M contain *LiUP* and studtite. *LiUP* was the only solid present after reacting *LiUP* with a solution at pH 11 and an initial H_2O_2 concentration of 0.5 M (Fig. 4).

Powder diffraction data collected for the various solids after dissolution experiments allowed identification of the phases in many cases, but some diffraction patterns contained peaks that correspond to one or more unknown phases. These may correspond to uranyl peroxide

compounds, including cluster compounds, as there is a dearth of powder diffraction data available for these. Figure 5 summarizes the phase composition of solids recovered after the seven-day reaction between the eight uranyl phosphate phases studied here with solutions containing varying amounts of hydrogen peroxide at pH values from 7 to 11. Controls were used to monitor the interaction between the uranyl phosphate phase and water at different pH values (designated *Water* in Figure 5) and the interaction between the uranyl phosphate phase and water with different concentrations of peroxide without pH adjustment (designated *Blank* in Figure 5). The pH ranged between 3 and 4 for each *Blank* reaction for all uranyl phosphate systems. In seven of the eight systems, the original uranyl phosphate phase, or its hydrated equivalent, was the only solid phase detected in the *Water* reactions containing no added H_2O_2. In the *CsUP* system, an unidentified phase was detected in most of the reactions, including the *CsUP* mixed with water only (Figure S82). The diffraction pattern of this phase does not match any known phase with possible compositions in the ICDD database. As this phase is observed when *CsUP* is mixed with water only with no pH adjustment, it is likely a higher hydrate of *CsUP*, similar to higher hydrates observed in the *CaUP*, *MgUP*, and *BaUP* systems. Autunite-type compounds commonly undergo hydration and dehydration reactions, and multiple hydrates have been described for many combinations of autunite-type sheets and interlayer cations (Dal Bo et al. 2016; Locock et al. 2004a, 2004b; Pekov et al. 2012, Plášil et al. 2010, Suzuki et al. 2005).

Studtite formed in almost all *Blank* control reactions in which uranyl phosphate solids were reacted with a solution containing H_2O_2 with no pH modification. In the *LiUP* and *NaUP* systems that had initial H_2O_2 concentrations greater than 0.1 M and no pH modifications, studtite is the only solid phase detected. In the *CsUP* and the *BaUP* systems, studtite only formed where

initial higher concentrations (0.1 – 1.0 M for *CsUP* and 0.5 – 1.0 M for *BaUP*) of H_2O_2 were present in the *Blank* reactions.

Most commonly, reaction of solid uranyl phosphates and aqueous solutions containing various H_2O_2 concentrations and with various pH values yielded a mixture of the original uranyl phosphate and studtite (Figure 5). Studtite did not form in reactions with initial peroxide concentrations greater than 0.10 M at pH 11. In the *RbUP*, *CsUP*, *CaUP*, and *BaUP* systems, phases unidentifiable by PXRD were detected in reactions conditions at high pH and peroxide content (PXRD patterns in Supporting Information). Little to no solid material remained in the *LiUP* and *NaUP* systems when the original material was reacted with solutions containing 1.0 M H_2O_2 at pH 11 (*LiUP*) and solutions containing 0.10 M to 1.0 M H_2O_2 at pH 10 and 11 (*NaUP*).

Counter Cation Effects on Uranyl Phosphate Dissolution

Uranyl peroxide cage clusters are anionic and, in many, the absolute value of the cluster charge is identical to the number of uranyl polyhedra in the cluster (Burns and Nyman 2018). The charges on uranyl peroxide clusters in aqueous systems and their salts are balanced by counter cations that are most commonly alkalis and less commonly alkaline earths. In the current aqueous systems containing added TEAOH, the TEA^+ cation can balance the charge of uranyl peroxide clusters. Each of the uranyl phosphate solids under study may also release alkali or alkaline earth cations to solution upon dissolution, and these may also serve to balance the charge of the uranyl peroxide clusters.

The solubility of crystals containing selected uranyl peroxide cage clusters have been studied previously (Peruski et al. 2016). Similar to trends of solubility of salts of transition metal polyoxometalates, salts of uranyl peroxide clusters are most soluble in solutions containing

lithium, are less soluble with increasing size of the monovalent counter cation, and are much less soluble in solutions containing divalent cations (Hickam et al. 2018; Nyman et al. 2010). The aqueous solubility of uranyl phosphate solids including those studied here is impacted by the specifics of the counter cations in the interlayer regions of their structures, although the effect will not be as large as for salts of uranyl peroxide cage clusters.

The dissolution behavior of eight synthetic uranyl phosphate members of the metaautunite subgroup were investigated here under 36 reaction conditions ranging in initial H_2O_2 concentration and pH. Dissolution of five phases with monovalent counter cations (Li^+, Na^+, K^+, Rb^+, and Cs^+) and three with divalent counter cations (Mg^{2+}, Ca^{2+}, Ba^{2+}) were examined and the results are summarized in Figure 6 (Tables S1 – S8). Uranium concentrations measured in solution by ICP-OES are represented in Figure 6 as a percentage of the total uranium in the original uranyl phosphate solid added to the aqueous system, as that was the only source of uranium. The same mass of uranyl phosphate solid was added to each experiment, but these compounds had different quantities of uranium in weight percent. The 30 mg of solid added contained from 44.6 wt.% uranium in *CsUP* to 54.2 wt.% uranium in *CaUP*.

In all uranyl phosphate systems, less than 0.5% of the total uranium is in solution in *Water* controls containing hydrogen peroxide with no pH adjustments. In the *Blank* control reactions with no added peroxide, less than 4.5% of the total uranium is in solution between pH 7 to 11 for all systems except *LiUP* and *NaUP*. At pH 11 in both cases, an increase in dissolution was observed where ~16% and ~8% of the original uranium in *LiUP* and *NaUP* is in solution, respectively.

In all eight uranyl phosphate systems, as both the initial peroxide concentration and pH of the solutions interacting with the solid increase, the amount of uranium dissolved into solution

also increases. At pH 7 and 8, less than 4% of the total uranium in the system is in solution under all peroxide conditions. The dissolution behaviors among the eight uranyl phosphate phases diverge between pH 9 and 11 and are summarized below.

No solid material remained in experiments containing *LiUP* and *NaUP* at pH 11 for solutions containing peroxide at initial concentrations of both 0.5 M and 1.0 M. In solutions containing 0.10 M peroxide at pH 11, ~88% of the uranium that was originally in *NaUP* was in solution, but less than 35% of the total uranium was in solution for experiments with the other uranyl phosphates. Between 51% and 59% of the total uranium in the *KUP*, *RbUP*, *MgUP*, and *CaUP* solids was in solutions containing 1.0 M peroxide at pH 11. For *CsUP* and *BaUP* in 1.0 M peroxide solutions at pH 11, only ~19% and ~37% of the total uranium was in solution, respectively.

Characterization of Phosphorous Species in Solution

Phosphate $(PO_4)^{3-}$ can bridge uranyl ions in uranyl peroxide cage clusters, such as $U_{20}P_6$, $[(UO_2)_{20}(O_2)_{27}(HPO_4)_6]^{26-}$ and $U_{124}P_{12}$, $[(UO_2)_{124}(O_2)_{152}(PO_4)_{16}(HPO_4)_8(H_2PO_4)_8(OH)_2(H_2O)_{24}]^{132-}$ (Burns and Nyman 2018; Dembowski et al. 2017a; Qiu et al. 2017). ^{31}P NMR studies were conducted here for select reactions to determine if the phosphate dissolved in solution was incorporated into uranyl peroxide cage clusters formed in these systems. Dembowski et al. performed ^{31}P NMR on aqueous solutions containing $U_{20}P_6$ and found that the phosphate bridges within the cluster produced an asymmetric signal at 15.23 ppm and free phosphate ions in solution yielded a signal at 3.31 ppm (Dembowski et al. 2017a). Figure 7 shows the ^{31}P NMR spectra of solutions resulting from the mixture of *LiUP*, *NaUP*, *KUP*, and *BaUP* with 0.5 M peroxide at pH 10

(*KUP*) and pH 11 (*LiUP*, *NaUP*, and *BaUP*). In each system, a single signal ranging between 3.68 ppm (*NaUP*) and 2.49 ppm (*KUP*) was observed, consistent with simple phosphate ions in solution. The variation of the phosphate signal is attributed to differences in pH (*KUP*) and ionic strength of the reaction solutions (Kost 1990; Seo et al. 1983).

Characterization of Uranyl Peroxide Species in Solution

Raman spectroscopy, ESI-MS and SAXS were used to characterize solutions with various peroxide concentrations at alkaline pH values into which one of eight synthetic uranyl phosphate phases were dissolved. All three techniques have previously been applied for characterizing uranyl peroxide cage clusters in solution (Burns and Nyman 2018), and ESI-MS and SAXS are well-established techniques for characterizing metal oxide clusters in solution (Burns and Nyman 2018; Dembowski et al. 2017a; Falaise and Nyman 2016; Miras et al. 2009; Qiu et al. 2014, 2017; Warzok et al. 2019).

Uranyl peroxide cage clusters in aqueous solution or the solid state typically produce Raman signals between 800 – 815 cm^{-1} due to the symmetric stretch of the uranyl ion, $v_1(UO_2)^{2+}$, and signals between 800 – 850 cm^{-1} owing to intermolecular peroxide vibrations, $v_{1\text{-}3}(O_2)^{2-}$ (Burns and Nyman 2018; Falaise and Nyman 2016; McGrail et al. 2014). Studtite, a mineral composed of uranyl peroxide chains, produces Raman signals at 819 cm^{-1} and 864 cm^{-1} due to the symmetric stretch of the uranyl ion and the stretch of the bridging peroxo ligands (Colmonero et al. 2017; Lobeck et al. 2019a). Uranyl triperoxide monomers $[(UO_2)(O_2)_3]^{4-}$ produce vibrational modes in the 700 – 750 cm^{-1} region (Dembowski et al. 2017b; Falaise and Nyman 2016; McGrail et al. 2014). Figure 8 shows a selected region of the Raman spectra of solutions resulting from the reaction between each uranyl phosphate phase and a solution at pH 11 that contained H_2O_2 with an initial concentration of 1.0 M. The remainder of the spectral

range contained no other peaks attributed to the uranyl peroxide species studied here. Spectra for all eight systems contain signals consistent with the presence of uranyl peroxide nanocluster species in solution with the $v_1(UO_2)^{2+}$ signal between 804 cm^{-1} and 810 cm^{-1} and the $v_2(O_2)^{2-}$ signal between 830 cm^{-1} and 847 cm^{-1} (Table 2). The observed spectral range of these peaks indicate different bonding environments of the uranyl and peroxide in these solutions (Bartlett and Cooney 1989; Eysel and Thym 1975), which may be due to formation of different uranyl peroxide cage clusters or potentially the interaction of cage clusters with different counter cations. For example, Raman spectra of U_{24} $[(UO_2)_{24}(O_2)_{24}(OH)_{24}]^{24-}$, U_{28} $[(UO_2)_{28}(O_2)_{42}]^{28-}$, and U_{60} $[(UO_2)_{60}(O_2)_{60}(OH)_{60}]^{60-}$ contain uranyl and peroxo peak positions of 810 cm^{-1} and 847 cm^{-1}, 807 cm^{-1} and 832 cm^{-1}, and 804 cm^{-1} and 842 cm^{-1}, respectively (Falaise and Nyman 2016; Hickam et al. 2018; Lobeck et al. 2019a, 2019b). Raman shifts can occur for uranyl and peroxo bands from the same uranyl peroxide cage cluster when different cations are introduced (Falaise and Nyman 2016). As the systems under study here contain several different counter cations, the Raman spectra do not permit definitive identification of uranyl peroxide cage clusters present in the solutions.

ESI-MS is a well-established technique for measuring the average mass of transition metal polyoxometalates in solution (Miras et al. 2009; Warzok et al. 2019) and it has been extensively applied to solutions containing uranyl peroxide nanoclusters (Burns and Nyman 2018; Hickam et al. 2018; Lobeck et al. 2019a, 2019b; McGrail et al. 2014; Qiu et al. 2012). Uranyl peroxide nanoclusters in solution are anionic and are associated with counter cations (Flynn et al. 2015; Gao et al. 2015; Sadergaski et al. 2018). ESI-MS of solutions containing uranyl peroxide cage clusters are complex with broad peaks in the range of 1200 to 4500 *m/z* (mass/charge) (McGrail et al. 2014; Qiu et al. 2012).

342 Figures 9 and 10 show representative ESI-MS of solutions resulting from the mixture of
343 each uranyl phosphate phase with peroxide in alkaline conditions in addition to predicted ESI-
344 MS patterns for U_{24} and U_{28} with various counter cations. ESI-MS data for solutions from all
345 reactions are in the Supporting Information. For each ESI-MS spectrum, peaks were assigned
346 charges between -6 and -3 and the average mass of the nanoclusters formed ranged from 7.9 kDa
347 to 11.5 kDa across all eight uranyl phosphate systems (Table 2).

348 Interpretation of the ESI-MS spectra for solutions containing uranyl peroxide cage
349 clusters is complicated because the charges of the cage clusters are high (-20 to -60 for U_{20} and
350 U_{60}). In addition, many counter cations are associated with the clusters in the spectrometer,
351 resulting in the observed charges, in this case, of -6 through -3. The solutions under study
352 contain substantial quantities of TEA^+ cations that originated from the TEAOH, as well as alkali
353 or alkaline earth cations released to solution by the dissolving uranyl phosphate solids. TEAOH
354 promotes a high aqueous solubility of uranyl peroxide nanoclusters, but poor crystallization
355 conditions, so it is difficult to determine the exact TEA^+ to alkali or alkaline earth cation ratio
356 associated with each cluster in each system. Given that the NMR spectra collected for selected
357 solutions are consistent with phosphate being the only phosphorous-bearing species in solution,
358 the uranyl ions within the clusters are likely bridged only by peroxide and hydroxyl groups.
359 Previously, dissolution of studtite in solutions containing TEAOH with and without added H_2O_2
360 produced U_{24} and U_{28} clusters in solution (Falaise and Nyman 2016; Lobeck et al. 2019a).
361 Simulations of ESI-MS spectra of U_{24} and U_{28} counterbalanced solely by TEA^+ or the alkali or
362 alkaline earth cation in the system are presented in Figures 9 and 10 for comparison to the
363 measured spectra. Calculated average masses for these simulated cluster species can be found in

Table 3. It is likely that the nanoclusters formed are counterbalanced by a mixture of TEA^+ and the alkali or alkaline earth cation.

In the *LiUP* system the measured mass of 10.2 kDa is consistent with U_{24} that is mostly charge-balanced by TEA^+ or U_{28} that is mostly charge balanced by Li^+. In the case of *NaUP*, the lower-mass cluster at 7.9 kDa is consistent with U_{24} with Na^+ as the only counter cation or a smaller cluster such as U_{20}. The larger cluster with mass 10.7 kDa is consistent with U_{24} in which the majority of the charge-balancing cations are TEA^+ or U_{28} with a mixture of TEA^+ and Na^+. For the single cluster indicated by ESI-MS in the *KUP* system, the observed mass of 10.3 kDa is consistent with U_{24} almost entirely charge balanced by TEA^+ or U_{28} mostly charge-balanced by K^+. In the case of the *RbUP* system, the observed mass at 10.8 kDa is consistent with U_{28} mostly charge balanced by Rb^+. For the *CsUP* system, the observed mass of 11.5 kDa is within experimental uncertainty with that expected for U_{28} charge-balanced by any combination of TEA^+ and Cs^+, but is more than 1.0 kDa higher than the mass calculated for U_{24} charge-balanced by either cation.

ESI-MS for the *CaUP* system indicate the presence of two clusters in solution. The smaller of these yielded a mass of 8.1 kDa, which is consistent with U_{24} mostly charge-balanced by Ca^{2+}. The larger has a mass of 11.1 kDa, which is consistent with U_{28} charge-balanced by dominantly TEA^+ and lesser Ca^{2+}. The ESI-MS for solution collected from the *MgUP* system yielded a mass of 11.1 kDa, which is consistent with U_{28} dominantly charge-balanced by TEA^+ with lesser Mg^{2+}. Finally, the cluster mass in the *BaUP* system is 10.3 kDa, which is consistent with U_{24} mostly charge-balanced by TEA^+ or U_{28} mostly charge-balanced by Ba^{2+}.

Given that the alkali cations are expected to interact more strongly with the uranyl peroxide clusters than TEA^+ (Burns and Nyman 2018; Falaise and Nyman 2016), it is likely that

all of the *LiUP*, *NaUP*, *KUP*, *RbUP* and *CsUP* systems contain U_{28} clusters, and that *NaUP* also contains U_{24} or possibly a cluster that is smaller than U_{24}, such as U_{20}. Solutions into which *MgUP*, *CaUP* and *BaUP* were dissolved likely contain U_{28} clusters, and the *CaUP* solution likely also contains U_{24}. Figure 11 summarizes all solutions in which uranyl peroxide nanoclusters were detected in solution by ESI-MS. In all eight systems, nanoclusters were observed in reaction solutions with increased peroxide concentrations and more alkaline pH. Clusters were detected in mildly alkaline environments at pH 8 in the *NaUP*, *KUP*, and *CaUP* systems. Clusters were also detected in solutions where 0.01 M peroxide was mixed with *NaUP*, *KUP*, and *MgUP* at pH values greater than 10.

SAXS measurement provide information on the size of the uranyl peroxide nanoclusters in solutions collected from each reaction system. The average radii of gyration (R_g) of the clusters in solution was determined by Guinier analysis of the low-*q* regions of the scattering curves (Figure 12) and are reported in Table 2. The average R_g measured ranged from 7.09 Å (*NaUP*) to 9.17 Å (*CsUP*) and are consistent with clusters in solution with a comparable size to U_{24} and U_{28} counterbalanced by various cations. Falaise et al. previously studied U_{28} clusters with different counter cations and reported that the R_g of U_{28} varied depending on the cations in the system (Falaise and Nyman 2016). A Li-U_{28} had a reported R_g of 7.53 Å, a K-U_{28} had a R_g of 7.30 Å, and a TEA-U_{28} had a R_g of 9.34 Å. The clusters reported in this study from the *LiUP* and *KUP* systems had measured R_g values of 7.83 Å and 8.86 Å, respectively. The larger R_g of clusters observed in these systems are consistent with the results from ESI-MS and point towards U_{28} forming in solution with a combination of TEA^+ and alkali or alkaline earth cations as a counterbalance. The systems with two species of clusters detected (*NaUP* and *CaUP*) had average R_g values of 7.09 Å and 7.53 Å, consistent with a mixture of U_{24} and U_{28} in solution.

410 *BaUP* had a reported R_g of 7.24 Å, which would point towards U_{24} clusters in solution
411 counterbalanced by mostly TEA^+ rather than U_{28} counterbalanced by mostly Ba^{2+}.
412
413 **Discussion**
414 The dissolution behaviors of eight synthetic uranyl phosphate phases in the metaautunite
415 subgroup in aqueous solutions containing H_2O_2 were investigated. Dissolution of the uranyl
416 phosphate solids generally provided uranium that self-assembled into uranyl peroxide clusters,
417 although the extent of nanocluster formation and the size and topology of the cluster formed was
418 influenced by the alkali or alkaline earth cations released from the interlayers of the uranyl
419 phosphate solids. The overall dissolution of uranyl phosphate phases containing Li^+, Na^+, K^+,
420 Rb^+, and Cs^+ increased as the hydrated radius of the cation increased and the ionic radius
421 decreased (Conway 1981). A similar trend is observed for dissolution of uranyl phosphates with
422 Mg^{2+}, Ca^{2+}, and Ba^{2+}. The highest dissolution of each uranyl phosphate phase occurs at higher
423 pH and higher peroxide concentrations (Figure 6). Congruently, uranyl peroxide nanoclusters
424 form in solution in systems exhibiting the most dissolution of the uranyl phosphate phase (Figure
425 11).
426 Studtite formed during alteration of the uranyl phosphate starting phases in the majority
427 of solution conditions studied here (Figure 5). Studtite has been found where spent nuclear fuel
428 (Armstrong et al. 2012), natural and synthetic UO_2 (Armstrong et al. 2012; Clarens et al. 2005;
429 Hanson et al. 2005), uranyl oxide hydroxide minerals (Forbes et al. 2011; Hanson et al. 2005),
430 and uranyl silicates (Forbes et al. 2011) come in contact with peroxide-bearing aqueous
431 solutions. The current findings demonstrate most uranyl phosphates in the metaautunite subgroup
432 are replaced by studtite during exposure to H_2O_2 over a wide range of pH. The interlayer cations

433 of the uranyl phosphate phase impact the extent of this transformation. Both *LiUP* and *NaUP*
434 completely transformed to studtite when exposed to 0.1 M to 1.0 M H_2O_2 for seven days (pH 3),
435 whereas studtite was only detected in two reaction conditions as a minor secondary phase in the
436 *BaUP* system.

437 Lobeck et al. investigated dissolution of studtite in alkaline aqueous solutions containing
438 peroxide (Lobeck et al. 2019a). They found little to no dissolution of studtite after seven days of
439 contact with a solution of TEAOH and H_2O_2 (0.01 M to 1.0 M) between pH 7 to 9. At pH 10,
440 17% to 42% of the original studtite in contact with 0.50 M and 1.0 M peroxide dissolved and
441 formed U_{28} nanoclusters in solution. At pH 11, between 8% and 64% of the original studtite
442 dissolved while in contact with 0.01 M to 0.10M peroxide, and complete dissolution of studtite
443 occurred in reactions where studtite was exposed to peroxide concentrations greater than 0.5 M.
444 In all of these reactions U_{28} nanoclusters formed in solution. These earlier findings are consistent
445 with the lack of studtite in any of the uranyl phosphate systems studied here at pH 11 with
446 peroxide concentrations greater than 0.10 M (Figure 5). In the *LiUP* and *NaUP* experiments, the
447 uranyl phosphate phase converted to studtite, and similar to the earlier studtite dissolution study,
448 complete dissolution of the solid occurred at pH 11 for reactions containing greater than 0.5 M
449 peroxide. In experiments where studtite was less prevalent, like those with *CsUP* and *BaUP*, less
450 solid dissolution was observed.

451 The alkali and alkaline earth cations contained within the uranyl phosphates under study
452 may influence the uranyl peroxide nanoclusters that form. Dissolution of studtite (Falaise and
453 Nyman 2016) and UO_2 (Hickam et al. 2018) (where studtite occurred as a secondary phase) in
454 alkaline peroxide-rich solutions produced different uranyl peroxide nanoclusters depending on
455 the counter cations in the system. Falaise et al. reported that studtite combined with excess

peroxide and various bases (LiOH, NaOH, KOH, NH_4OH, and TEAOH) resulted in predominantly U_{28}, and mixtures of U_{28} and U_{20} (Na^+) and U_{28} and U_{32} (NH_4^+) were observed (Falaise and Nyman 2016). Hickam et al. described the formation of a variety of uranyl peroxide nanoclusters after dissolution of UO_2 in peroxide rich solutions containing LiOH, NaOH, and KOH (Hickam et al. 2018). In systems containing Li^+ and K^+, U_{28} was predominant. In the Na^+-rich system, U_{20}, U_{24}, U_{28}, and U_{32} formed dependent on solution pH and the concentration of NaOH. The average masses of the uranyl peroxide clusters formed in the current study are similar to those of U_{24} and U_{28} (Figure 9 and Figure 10), consistent with the two previous studies. Two species of uranyl peroxide nanocluster were detected in the *NaUP* and *CaUP* system, which is also consistent with both of the Na^+-bearing reactions studied above.

Implications

Uranyl phosphates of the autunite group usually exhibit low aqueous solubilities. The current study indicates the formation of soluble uranyl peroxide cage clusters from sparingly soluble uranyl phosphate minerals has the potential to greatly impact the fate and transport of uranium in the environment. The Medvědín uranium deposit in northern Bohemia, Czech Republic (Plášil et al. 2009), and the Menzenschwand deposit in the Schwarzwald in southwest Germany (Göb et al. 2013), both contain large abundances of uranyl phosphate and arsenate supergene alteration mineral phases. In natural systems, small amounts of peroxide are often produced by the radiolysis of groundwater due to the ionizing radiation associated with uranium minerals and studtite is often found as a secondary phase (Colmenero et al. 2017; Forbes et al. 2011; Sattonnay 2001). The influence of peroxide on these deposits and an alkaline shift in pH could greatly affect the solubility of the uranium in these systems. Uranyl peroxide cage clusters self-

assemble in alkaline solutions containing peroxide and alkali or alkaline earth cations and uranyl ions and have been observed to co-exist with studtite under certain environmental conditions (Lobeck 2019a). The results of our current experiments demonstrate that formation of uranyl peroxide cage clusters in aqueous solution accompanies extensive dissolution of uranyl phosphates of the autunite group and metaautunite subgroup in alkaline solutions containing H_2O_2. The greatest dissolution of uranyl phosphates in our experiments occurred for those that contained cations with larger hydration radii, *LiUP* and *NaUP*. Understanding the stability of uranyl phosphate and uranyl peroxide complexes under all pH environments is of increasing interest with regard to uranium mining and spent nuclear fuel disposal.

Acknowledgments

This research was funded by the U.S. Department of Energy, National Nuclear Security Administration (DE–NA0003763). We thank the Center for Environmental Science and Technology, Materials Characterization Facility, and Mass Spectrometry and Proteomics Facility at the University of Notre Dame for the instrumentation used in this work. Additional thanks are extended to Aaron S. Donahue for his assistance with MATLAB and development of the colorplot figures.

References

Abrefah, J., Marschman, S.C., Jenson, E.D. (1998) Examination of the Surface Coatings Removed from K-East Basin Fuel Elements. Pacific Northwest National Laboratory Report-11806.

Armstrong, C.R., Nyman, M., Shvareva, T., Sigmon, G.E., Burns, P.C., Navrotsky, A. (2012) Uranyl peroxide enhanced nuclear fuel corrosion in seawater. Proceedings of the National Academy of Sciences of the United States of America, 109, 1874-1877.

Astilleros, J.M., Pinto, A.J., Goncalves, M.A., Sanchez-Pastor, N., Fernandez-Diaz, L. (2013) In Situ Nanoscale Observations of Metatorbernite Surfaces Interacted with Aqueous Solutions. Environmental Science & Technology, 47, 2636-2644.

Bartlett, J.R., Cooney, R.P. (1989) On the determination of uranium oxygen bond lengths in dioxouranium(VI) compounds by Raman. Journal of Molecular Structure, 193, 295-300.

Buck, E.C., Brown, N.R., Dietz, N.L. (1996) Contaminant uranium phases and leaching at the Fernald site in Ohio. Environmental Science & Technology, 30, 81-88.

Burns, P.C., Hughes, K.A. (2003) Studtite, (UO2)(O2)(H2O)2 (H2O)2: The first structure of a peroxide mineral. American Mineralogist, 88, 1165-1168.

Burns, P.C. (2005) U^{6+} minerals and inorganic compounds: Insights into an expanded structural hierarchy of crystal structures. Canadian Mineralogist, 43, 1839-1894.

Burns, P.C. (2011) Nanoscale uranium-based cage clusters inspired by uranium mineralogy. Mineralogical Magazine, 75, 1-25.

Burns, P.C., Nyman, M. (2018) Captivation with encapsulation: a dozen years of exploring uranyl peroxide capsules. Dalton Transactions, 47, 5916-5927.

Burns, P.C., Ewing, R.C., Navrotsky, A. (2012) Nuclear Fuel in a Reactor Accident. Science, 335, 1184-1188.

Clarens, F., de Pablo, J., Casas, I., Gimenez, J., Rovira, M., Merino, J., Cera, E., Bruno, J., Quinones, J., Martinez-Esparza, A. (2005) The oxidative dissolution of unirradiated UO2 by hydrogen peroxide as a function of pH. Journal of Nuclear Materials, 345, 225-231.

524 Colmenero, F., Bonales, L.J., Cobos, J., Timon, V. (2017) Study of the thermal stability of
525 studtite by *in situ* Raman spectroscopy and DFT calculations. Spetrochimica Acta Part A:
526 Molecular and Biomolecular Spectroscopy, 174, 245-253.
527 Conway, B.E. (1981) Ionic hydration in chemistry and biophysics. Amsterdam, Elsevier
528 Scientific Pub. Co. New York
529 Dal Bo, F., Hatert, F., Mees, F., Philippo, S., Baijot, M., Fontaine, F. (2016) Crystal structure of
530 bassetite and saléeite: new insight into autunite-group minerals. European Journal of
531 Mineralology, 28, 663-675.
532 Dembowski, M., Colla, C.A., Yu, P., Qiu, J., Szymanowski, J.E.S., Casey, W.H., Burns, P.C.
533 (2017a) The Propensity of Uranium-Peroxide Systems to Preserve Nanosized
534 Assemblies. Inorganic Chemistry, 56, 9602-9608.
535 Dembowski, M., Bernales, V., Qiu, J.E., Hickam, S., Gaspar, G., Gagliardi, L., Burns, P.C.
536 (2017b) Computationally-Guided Assignment of Unexpected Signals in the Raman
537 Spectra of Uranyl Triperoxide Complexes. Inorganic Chemistry, 56, 1574-1580.
538 Dzik, E.A.; Lobeck, H.L., Zhang, L., Burns, P. C. (2017a) Thermodynamic properties of
539 phosphate members of the meta-autunite group: A high-temperature calorimetric study.
540 Journal of Chemical Thermodynamics, 114, 165-171.
541 Dzik, E.A., Lobeck, H.L., Zhang, L., Burns, P.C. (2017b) Thermodynamic characterization of
542 synthetic autunite. American Mineralogist, 102, 1977-1980.
543 Eysel, H.H., Thym, S. (1975) Raman-spectra of peroxides. Zeitschrift Fur Anorganische Und
544 Allgemeine Chemie, 411, 97-102.
545 Falaise, C., Nyman, M. (2016) The Key Role of U-28 in the Aqueous Self-Assembly of Uranyl
546 Peroxide Nanocages. Chemistry-a European Journal, 22, 14678-14687.

547 Fanizza, M.F., Yoon, H., Zhang, C.Y., Oostrom, M., Wietsma, T.W., Hess, N.J., Bowden, M.E.,
548 Strathmann, T.J., Finneran, K.T., Werth, C.J. (2013) Pore-scale evaluation of uranyl
549 phosphate precipitation in a model groundwater system. Water Resources Research, 49,
550 874-890.
551 Fernelius, W.C., Detling, K.D. (1934) Preparation of Crystals of Sparingly Soluble Salts. Journal
552 of Chemical Education, 176-178.
553 Flynn, S.L., Szymanowski, J.E.S., Gao, Y.Y., Liu, T.B., Burns, P.C., Fein, J.B. (2015)
554 Experimental measurements of U60 nanocluster stability in aqueous solution.
555 Geochimica Et Cosmochimica Acta, 156, 94-105.
556 Forbes, T.Z., Horan, P., Devine, T., McInnis, D., Burns, P.C. (2011) Alteration of dehydrated
557 schoepite and soddyite to studtite, (UO2)(O-2)(H2O)(2) (H2O)(2). American
558 Mineralogist, 96, 202-206.
559 Fuller, C.C., Bargar, J.R., Davis, J.A., Piana, M.J. (2002) Mechanisms of uranium interactions
560 with hydroxyapatite: Implications for groundwater remediation. Environmental Science
561 & Technology, 36, 158-165.
562 Gao, Y.Y., Haso, F., Szymanowski, J.E.S., Zhou, J., Hu, L., Burns, P.C., Liu, T.B. (2015)
563 Selective Permeability of Uranyl Peroxide Nanocages to Different Alkali Ions: Influences
564 from Surface Pores and Hydration Shells. Chemistry-a European Journal, 21, 18785-
565 18790.
566 Göb, S., Gühring, J.E., Bau, M., Markl, G. (2013) Remobilization of U and REE and the
567 formation of secondary minerals in oxidized U deposits. American Mineralogist, 98, 530-
568 548.

569 Gorman-Lewis, D., Shvareva, T., Kubatko, K.A., Burns, P.C., Wellman, D.M., McNamara, B.,
570 Szymanowski, J.E.S., Navrotsky, A., Fein, J.B. (2009) Thermodynamic Properties of
571 Autunite, Uranyl Hydrogen Phosphate, and Uranyl Orthophosphate from Solubility and
572 Calorimetric Measurements. Environmental Science & Technology, 43, 7416-7422.
573 Gudavalli, R., Katsenovich, Y., Wellman, D. (2018) Quantification of kinetic rate law
574 parameters for the dissolution of natural autunite in the presence of aqueous bicarbonate
575 ions at high concentrations. Journal of Environmental Radioactivity, 190, 1-9.
576 Hanson, B., McNamara, B., Buck, E., Friese, J., Jenson, E., Krupka, K., Arey, B. (2005)
577 Corrosion of commercial spent nuclear fuel. 1. Formation of studtite and metastudtite.
578 Radiochimica Acta, 93, 159-168.
579 Hickam, S., Aksenov, S.M., Dembowski, M., Perry, S.N., Traustason, H., Russell, M., Burns,
580 P.C. (2018) Complexity of Uranyl Peroxide Cluster Speciation from Alkali-Directed
581 Oxidative Dissolution of Uranium Dioxide. Inorganic Chemistry, 57, 9296-9305.
582 Hickam, S., Breier, J., Cripe, J., Cole, E., Burns, P.C. (2019) Effects of H_2O_2 Concentration on
583 Formation of Uranyl Peroxide Species Probed by Dissolution of Uranium Nitride and
584 Uranium Dioxide. Inorganic Chemistry, DOI: 10.1021/acs.inorgchem.9b00231.
585 Ilavsky, J., Jemian, P.R. (2009) Irena: tool suite for modeling and analysis of small-angle
586 scattering. Journal of Applied Crystallography, 42, 347-353.
587 Kost, G.J. (1990) pH standardization for P-31 magnetic-resonance heart spectroscopy at different
588 temperatures. Magnetic Resonance in Medicine, 14, 496-506.
589 Krivovichev, S.V., Plášil, J. (2013) Mineralogy and crystallography of uranium. Uranium: From
590 Cradle to Grave. Mineralogical Association of Canada Short Courses, 43, 15 - 119.

591 Lammers, L.N., Rasmussen, H., Adilman, D., deLemos, J.L., Zeeb, P., Larson, D. G., Quicksall,
592 A.N. (2017) Groundwater uranium stabilization by a metastable hydroxyapatite. Applied
593 Geochemistry, 84, 105-113.
594 Lobeck, H.L., Isner, J.K, Burns, P. C. (2019a) Transformation of the Uranyl Peroxide Studtite,
595 $[(UO_2)(O_2)(H_2O)_2](H_2O)_2$, to Soluble Nanoscale Cage Clusters. Inorganic Chemistry, 58,
596 6781-6789.
597 Lobeck, H.L., Traustason, H., Julien, P.A., FitzPatrick, J.R., Mana, S., Szymanowski, J.E.S.,
598 Burns, P.C. (2019b) *In situ* Raman spectroscopy of uranyl peroxide nanoscale cage
599 clusters under hydrothermal conditions. Dalton Transactions, 48, 7755-7765.
600 Locock, A.J., Burns, P.C., Duke, M.J.M., Flynn, T.M. (2004a) Monovalent cations in structures
601 of the meta-autunite group. Canadian Mineralogist, 42, 973-996.
602 Locock, A.J., Burns, P.C., Flynn, T.M. (2004b) Divalent Transition Metals and Magnesium in
603 Structures that Contain the Autunite-type Sheet. Canadian Mineralogist, 42, 1699-1718.
604 Locock, A.J. (2007) Trends in Actinide Compounds with the Autunite Sheet-Anion Topology.
605 Proceedings of the Russian Mineral Society, 136, 115-137.
606 Magnin, M., Jegou, C., Caraballo, R., Broudic, V., Tribet, M., Peuget, S., Talip, Z. (2015)
607 Oxidizing dissolution mechanism of an irradiated MOX fuel in underwater aerated
608 conditions at slightly acidic pH. Journal of Nuclear Materials, 462, 230-241.
609 Mallon, C., Walshe, A., Forster, R.J., Keyes, T.E., Baker, R.J. (2012) Physical Characterization
610 and Reactivity of the Uranyl Peroxide $UO_2(\eta^2\text{-}O_2)(H_2O)_2$ center dot $2H_2O$: Implications
611 for Storage of Spent Nuclear Fuels. Inorganic Chemistry, 51, 8509-8515.

McGrail, B.T., Sigmon, G.E., Jouffret, L.J., Andrews, C.R., Burns, P.C. (2014) Raman Spectroscopic and ESI-MS Characterization of Uranyl Peroxide Cage Clusters. Inorganic Chemistry, 53, 1562-1569.

Mehta, V.S., Maillot, F., Wang, Z.M., Catalano, J.G., Giammar, D.E. (2014) Effect of co-solutes on the products and solubility of uranium(VI) precipitated with phosphate. Chemical Geology, 364, 66-75.

Mehta, V.S., Maillot, F., Wang, Z.M., Catalano, J.G., Giammar, D.E. (2015) Transport of U(VI) through sediments amended with phosphate to induce in situ uranium immobilization. Water Research, 69, 307-317.

Miras, H.N., Wilson, E.F., Cronin, L. (2009) Unravelling the complexities of inorganic and supramolecular self-assembly in solution with electrospray and cryospray mass spectrometry. Chemical Communications (Cambridge, U. K.), 11, 1297-1311.

Munasinghe, P.S., Madden, M.E.E., Brooks, S.C., Madden, A.S.E. (2015) Dynamic interplay between uranyl phosphate precipitation, sorption, and phase evolution. Applied Geochemistry, 58, 147-160.

Murakami, T., Ohnuki, T., Isobe, H., Sato, T. (1997) Mobility of uranium during weathering. American Mineralogist, 82, 888-899.

Nyman, M., Rodriguez, M.A., Campana, C.F. (2010) Self-Assembly of Alkali-Uranyl-Peroxide Clusters. Inorganic Chemistry, 49, 7748-7755.

Odoh, S.O., Shamblin, J., Colla, C.A., Hickam, S., Lobeck, H.L., Lopez, R.A.K., Olds, T., Szymanowski, J.E.S., Sigmon, G.E., Neuefeind, J., Casey, W.H., Lang, M., Gagliardi, L., Burns, P.C. (2016) Structure and Reactivity of X-ray Amorphous Uranyl Peroxide, U_2O_7. Inorganic Chemistry, 55, 3541-3546.

635 Pekov, I.V., Levitskiy, V.V., Krivovichev, S.V., Zolotarev, A.A., Bryzgalov, I.A., Zadov A.E.,
636 Chukanov, N.V. (2012) New nickel-uranium-arsenic mineral species from the oxidation
637 zone of the Belorechenskoye deposit, Northern Caucasus, Russia: I. Rauchite,
638 Ni(UO2)2(AsO4)2dot10H2O, a member of the autunite group. European Journal of
639 Mineralogy, 24, 913-922.
640
641 Perdrial, N., Vazquez-Ortega, A., Wang, G.H., Kanematsu, M., Mueller, K.T., Um, W., Steefel,
642 C.I., O'Day, P.A., Chorover, J. (2018) Uranium speciation in acid waste-weathered
643 sediments: The role of aging and phosphate amendments. Applied Geochemistry, 89,
644 109-120.
645 Peruski, K.M., Bernales, V., Dembowski, M., Lobeck, H.L., Pellegrini, K.L., Sigmon, G.E.,
646 Hickam, S.M., Wallace, C.M., Szymanowski, J.E.S., Balboni, E., Gagliardi, L., Burns,
647 P.C. (2016) Uranyl Peroxide Cage Cluster Solubility in Water and the Role of the
648 Electrical Double Layer. Inorganic Chemistry, 56, 1333 – 1339.
649 Plášil, J., Sejkora, J., Čejka, J., Skoda, R., Goliaš, V. (2009) Supergene mineralization of the
650 Medvědín uranium deposit, Krkonoše Mountains, Czech Republic. Journal of
651 Geosciences, 54, 15-56.
652 Plášil, J., Sejkora, J., Čejka, J., Novák, M., Viñals, J., Ondruš, P., Veselovsky, F., Škácha, P.,
653 Jehlicka, J., Goliaš, V., Hloušek, J. (2010) Metarauchite, Ni(UO2)2(AsO4)2•8H2O,
654 From Jáchymov, Czech Republic, and Schneeberg, Germany: A New Member Of The
655 Autunite Group. Canadian Mineralogist, 48, 335-350.
656 Qiu, J., Burns, P.C. (2013) Clusters of Actinides with Oxide, Peroxide, or Hydroxide Bridges.
657 Chemical Reviews, 113, 1097-1120.

658 Qiu, J., Ling, J., Sui, A., Szymanowski, J.E.S., Simonetti, A., Burns, P.C. (2012) Time-Resolved
659 Self-Assembly of a Fullerene-Topology Core-Shell Cluster Containing 68 Uranyl
660 Polyhedra. Journal of the American Chemical Society, 134, 1810-1816.
661 Qiu, J., Ling, J., Jouffret, L., Thomas, R., Szymanowski, J.E.S., Burns, P.C. (2014) Water-
662 soluble multi-cage super tetrahedral uranyl peroxide phosphate clusters. Chemical
663 Science, 5, 303-310.
664 Qiu, J., Spano, T.L., Dembowski, M., Kokot, A.M., Szymanowski, J.E.S., Burns, P.C. (2017)
665 Sulfate-Centered Sodium-lcosahedron-Templated Uranyl Peroxide Phosphate Cages with
666 Uranyl Bridged by mu-eta(1):eta(2) Peroxide. Inorganic Chemistry, 56, 1874-1880.
667 Raicevic, S., Wright, J.V., Veljkovic, V., Conca, J.L. (2006) Theoretical stability assessment of
668 uranyl phosphates and apatites: Selection of amendments for in situ remediation of
669 uranium. Science of the Total Environment, 355, 13-24.
670 Reynolds, J.G., Cooke, G.A., Page, J.S., Warrant, R.W. (2018) Uranium-bearing phases in
671 Hanford nuclear waste. Journal of Radioanalytical and Nuclear Chemistry, 316, 289-299.
672 Sadergaski, L.R., Stoxen, W., Hixon, A.E. (2018) Uranyl peroxide nanocluster (U-60)
673 persistence and sorption in the presence of hematite. Environmental Science &
674 Technology, 52, 3304-3311.
675 Sattonnay, G., Ardois, C., Corbel, C., Lucchini, J.F., Barthe, M.F., Garrido, F., Gosset, D. (2001)
676 Alpha-radiolysis effects on UO2 alteration in water. Journal of Nuclear Materials, 288,
677 11-19.
678 Seo, Y., Murakami, M., Watari, H., Imai, Y., Yoshizaki, K., Nishikawa, H., Morimoto, T. (1983)
679 Intracellular pH determination by a P-31-NMR Technique - The 2nd dissociation-
680 constant of phosphoric-acid in a biological system. Journal of Biochemistry, 94, 729-734.

681 Singer, D.M., Zachara, J.M., Brown, G.E. (2009) Uranium Speciation As a Function of Depth in
682 Contaminated Hanford Sediments - A Micro-XRF, Micro-XRD, and Micro- And Bulk-
683 XAFS Study. Environmental Science & Technology, 43, 630-636.
684 Suzuki, Y., Sato, T., Isobe, H., Kogure, T., Murakami, T. (2005) Dehydration processes in the
685 meta-autunite group minerals meta-autunite, metasaleeite, and metatorbernite. American
686 Mineralogist, 90, 1308-1314.
687 Unruh, D.K., Burtner, A., Pressprich, L., Sigmon, G.E., Burns, P.C. (2010) Uranyl peroxide
688 closed clusters containing topological squares. Dalton Transactions, 39, 5807-5813.
689 VanHaverbeke, L., Vochten, R., VanSpringel, K. (1996) Solubility and spectrochemical
690 characteristics of synthetic chernikovite and meta-ankoleite. Mineralogical Magazine, 60,
691 759-766.
692 Warzok, U., Mahnke, L.K., Bensch, W. (2019) Soluble Hetero-Polyoxovanadates and Their
693 Solution Chemistry Analyzed by Electrospray Ionization Mass Spectrometry. Chemistry-
694 a European Journal, 25, 1405-1419.
695 Wellman, D.M., Icenhower, J.P., Gamerdinger, A.P., Forrester, S.W. (2006a) Effects of pH,
696 temperature, and aqueous organic material on the dissolution kinetics of meta-autunite
697 minerals, (Na, Ca)(2-1) (UO2)(PO4) (2)center dot 3H(2)O. American Mineralogist, 91,
698 143-158.
699 Wellman, D.M., Icenhower, J.P., Owen, A.T. (2006b) Comparative analysis of soluble phosphate
700 amendments for the remediation of heavy metal contaminants: Effect on sediment
701 hydraulic conductivity. Environmental Chemistry, 3, 219-224.

Wellman, D.M., Pierce, E.M., Valenta, M.M. (2007a) Efficacy of soluble sodium tripolyphosphate amendments for the in-situ immobilisation of uranium. Environmental Chemistry, 4, 293-300.

Wellman, D.M., Gunderson, K.M., Icenhower, J.P., Forrester, S.W. (2007b) Dissolution kinetics of synthetic and natural meta-autunite minerals, X-3-n((n)+) (UO2)(PO4) (2) center dot xH(2)O, under acidic conditions. Geochemistry Geophysics Geosystems, 8, 16.

Wellman, D.M., Glovack, J.N., Parker, K., Richards, E.L., Pierce, E.M. (2008) Sequestration and retention of uranium(VI) in the presence of hydroxylapatite under dynamic geochemical conditions. Environmental Chemistry, 5, 40-50.

List of Figure Captions

Figure 1. Polyhedral representation of meta-autunite sheet type structure. Yellow polyhedra correspond to uranium, purple polyhedra correspond to phosphate, and green spheres represent countercations in the interlayer.

Figure 2. Polyhedral representation of uranyl peroxide nanoclusters U_{20}, U_{24}, U_{28}, U_{30}, and U_{32}.

Figure 3. Schematic of slow mixing by liquid diffusion setup.

Figure 4. PXRD spectra of solids recovered after a seven – day reaction between *LiUP* and 0.50 M H_2O_2 at varying pH values.

724 **Figure 5.** Graphical representation of solid phases identified by PXRD after a seven-day reaction
725 between each mineral phase and solutions containing hydrogen peroxide (0.01 M – 1.0 M) at
726 varying pH values. Green squares correspond to the identification of the original phase or a
727 hydrated equivalent. Yellow squares correspond to the identification of uranyl peroxide, studtite.
728 Grey squares correspond to the detection of unidentified secondary phases. White squares
729 represent system where there was little to no solid remaining.

730

731 **Figure 6.** Color graph of U dissolved (%) for each uranyl phosphate phase in solutions
732 containing peroxide (0.01 M to 1.0 M) from pH 7 to 11.

733

734 **Figure 7.** ^{31}P NMR of reaction solutions resulting from the mixture of LiUP, NaUP, KUP, and
735 BaUP with 0.5M peroxide at pH 10 (KUP) and pH 11 (LiUP, NaUP, and BaUP).

736

737 **Figure 8.** Raman spectra of solutions resulting from the mixture of each uranyl phosphate
738 mineral phase with 1.0 M peroxide at pH 11.

739

740 **Figure 9.** Representative ESI-MS spectra of cluster species detected in the *LiUP*, *NaUP*, *KUP*,
741 and *RbUP* systems. Simulated ESI-MS data for U_{24} and U_{28} nanoclusters associated with the
742 various counter cations and TEA^+ are shown below each measured spectrum.

743

744 **Figure 10.** Representative ESI-MS spectra of cluster species detected in the *CsUP*, *MgUP*,
745 *CaUP*, and *BaUP* systems. Simulated ESI-MS data for U_{24} and U_{28} nanoclusters associated with
746 the various counter cations and TEA^+ are shown below each measured spectrum.

747

748 **Figure 11.** Graphical representation of environments where uranyl peroxide nanoclusters were
749 detected in solution for each uranyl phosphate system.

750

751 **Figure 12.** SAXS data of solutions resulting from the mixture of each uranyl phosphate phase
752 with 1.0 M peroxide at pH 11.

753

754 **Tables**

755 **Table 1.** Uranyl phosphate phases in the meta-autunite group and their hydrated equivalent
756 identified in these studies

Sample Name	Mineral Name	Formula	PXRD Powder Diffraction File #
LiUP	-	$Li(UO_2)(PO_4)(H_2O)_4$	04 014 3756
NaUP	Metanautroautunite	$Na(UO_2)(PO_4)(H_2O)_3$	04 014 3757
KUP	Meta-ankoleite	$K(UO_2)(PO_4)(H_2O)_3$	00 060 0284
RbUP	-	$Rb(UO_2)(PO_4)(H_2O)_3$	04 014 3761
CsUP	-	$Cs(UO_2)(PO_4)(H_2O)_{2.5}$	04 014 3766
MgUP	Metasaléeite	$Mg(UO_2)_2(PO_4)_2(H_2O)_8$	00 053 0012
	Saléeite	$Mg(UO_2)_2(PO_4)_2(H_2O)_{10}$	00 053 0011
CaUP	Meta-autunite	$Ca(UO_2)_2(PO_4)_2(H_2O)_6$	00 012 0423
	Autunite	$Ca(UO_2)_2(PO_4)_2(H_2O)_{10}$	00 041 1353
BaUP	Metauranocircite II	$Ba(UO_2)_2(PO_4)_2(H_2O)_6$	00 017 0759
	Metauranocircite I	$Ba(UO_2)_2(PO_4)_2(H_2O)_8$	00 036 0407

757
758

This is a preprint, the final version is subject to change, of the American Mineralogist (MSA)
Cite as Authors (Year) Title. American Mineralogist, in press.
DOI: https://doi.org/10.2138/am-2020-7106

759 **Table 2.** Summary of the characterization of solutions resulting from the seven-day reaction
760 between uranyl phosphate phases and hydrogen peroxide at alkaline pH

Uranyl Phosphate	Raman		ESI-MS	SAXS
	$\nu_s(UO_2)^{2+}$ (cm^{-1})	$\nu_2(O_2)^{2-}$ (cm^{-1})	Average Mass (kDa)	R_g (Å)
LiUP	808	844	10.2	7.83
NaUP	808	828	7.9, 10.7	7.09
KUP	806	834	10.3	8.86
RbUP	805	832	10.8	8.28
CsUP	806	830	11.5	9.17
MgUP	806	832	11.1	7.76
CaUP	811	848	8.1, 11.1	7.53
BaUP	808	833	10.3	7.24

761

762

763 **Table 3.** Calculated average mass of simulated U_{24} and U_{28} clusters with net charges between -6
764 and -3 counterbalanced by various cations compared to the measured average mass of clusters in
765 each reaction condition from ESI-MS.

Cation	Calculated Average Mass of Simulated Clusters (kDa)		Measured Average Mass of Cluster in System (kDa)
	U_{24}	U_{28}	
TEA^+	10.2	12.0	-
Li^+	7.8	9.1	10.2
Na^+	8.1	9.4	7.9, 10.7
K^+	8.4	9.8	10.3
Rb^+	9.3	10.9	10.8
Cs^+	10.2	12.0	11.5
Mg^{2+}	7.9	9.2	11.1
Ca^{2+}	8.1	9.4	8.1, 11.1
Ba^{2+}	9.0	10.5	10.3

This is a preprint, the final version is subject to change, of the American Mineralogist (MSA)
Cite as Authors (Year) Title. American Mineralogist, in press.
DOI: https://doi.org/10.2138/am-2020-7106

766

767 **Figures**

768

Figure 1

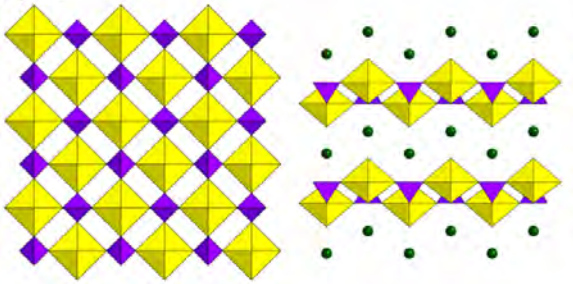

769

770

Figure 2

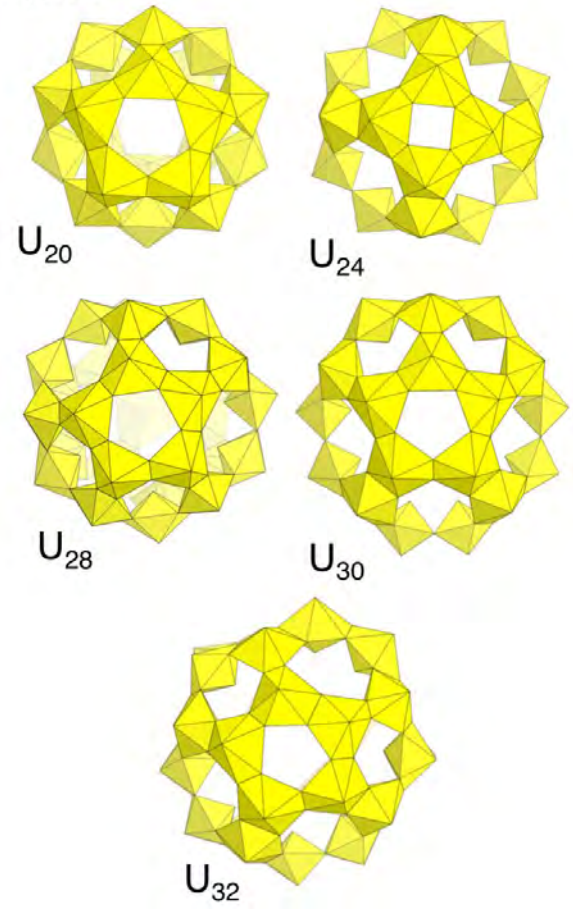

771

772

This is a preprint, the final version is subject to change, of the American Mineralogist (MSA)
Cite as Authors (Year) Title. American Mineralogist, in press.
DOI: https://doi.org/10.2138/am-2020-7106

Figure 3

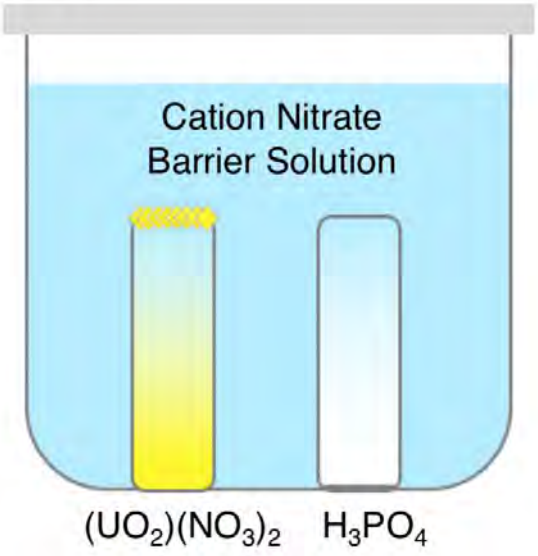

773

774

Figure 4

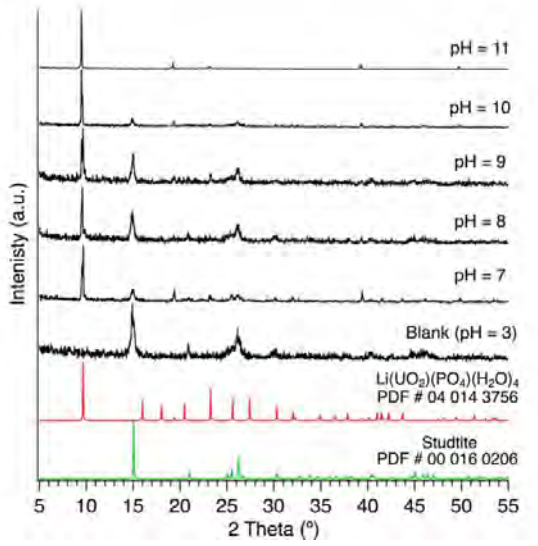

775

776

This is a preprint, the final version is subject to change, of the American Mineralogist (MSA)
Cite as Authors (Year) Title. American Mineralogist, in press.
DOI: https://doi.org/10.2138/am-2020-7106

Figure 5

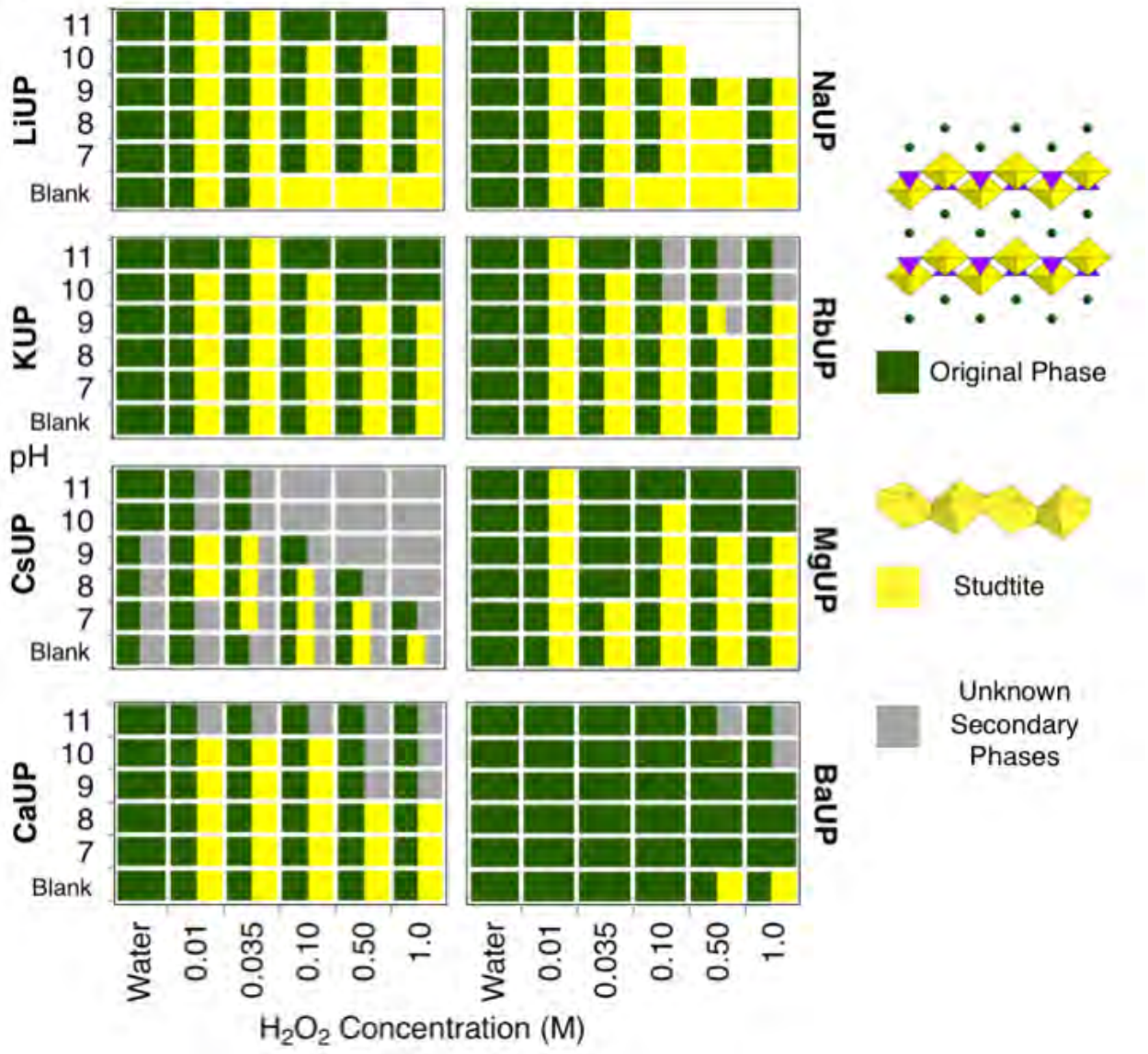

777

778

This is a preprint, the final version is subject to change, of the American Mineralogist (MSA)
Cite as Authors (Year) Title. American Mineralogist, in press.
DOI: https://doi.org/10.2138/am-2020-7106

Figure 6

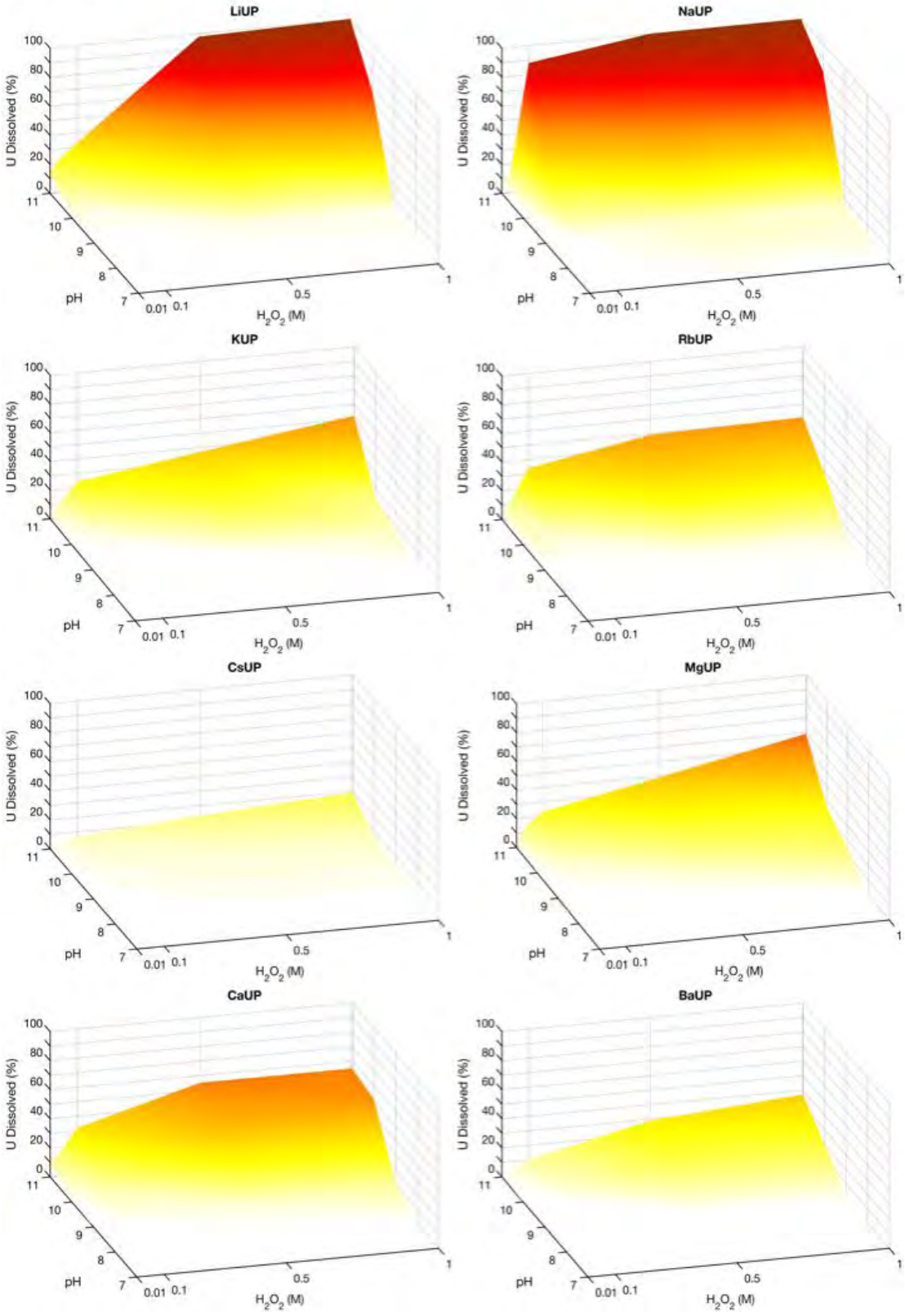

779

This is a preprint, the final version is subject to change, of the American Mineralogist (MSA)
Cite as Authors (Year) Title. American Mineralogist, in press.
DOI: https://doi.org/10.2138/am-2020-7106

Figure 7

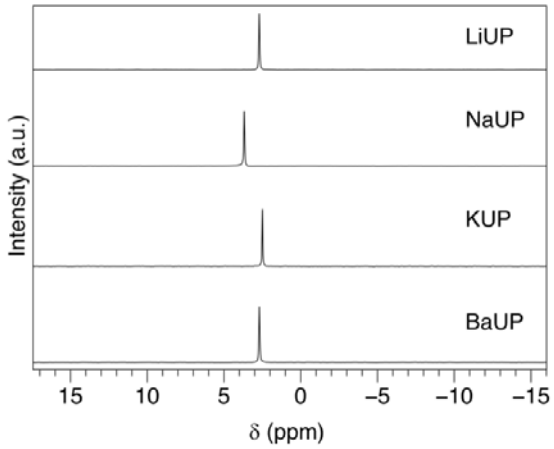

780

781

Figure 8

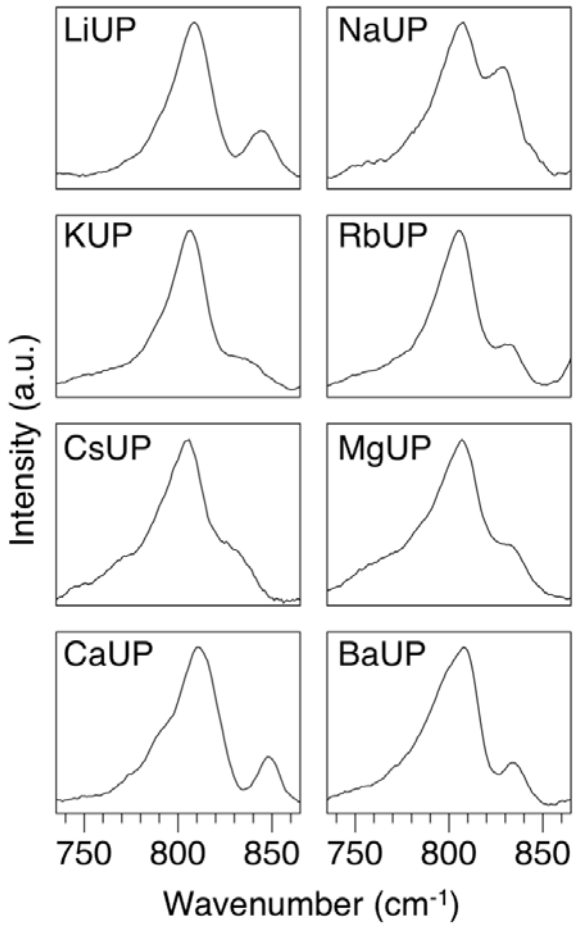

782

783

This is a preprint, the final version is subject to change, of the American Mineralogist (MSA)
Cite as Authors (Year) Title. American Mineralogist, in press.
DOI: https://doi.org/10.2138/am-2020-7106

Figure 9

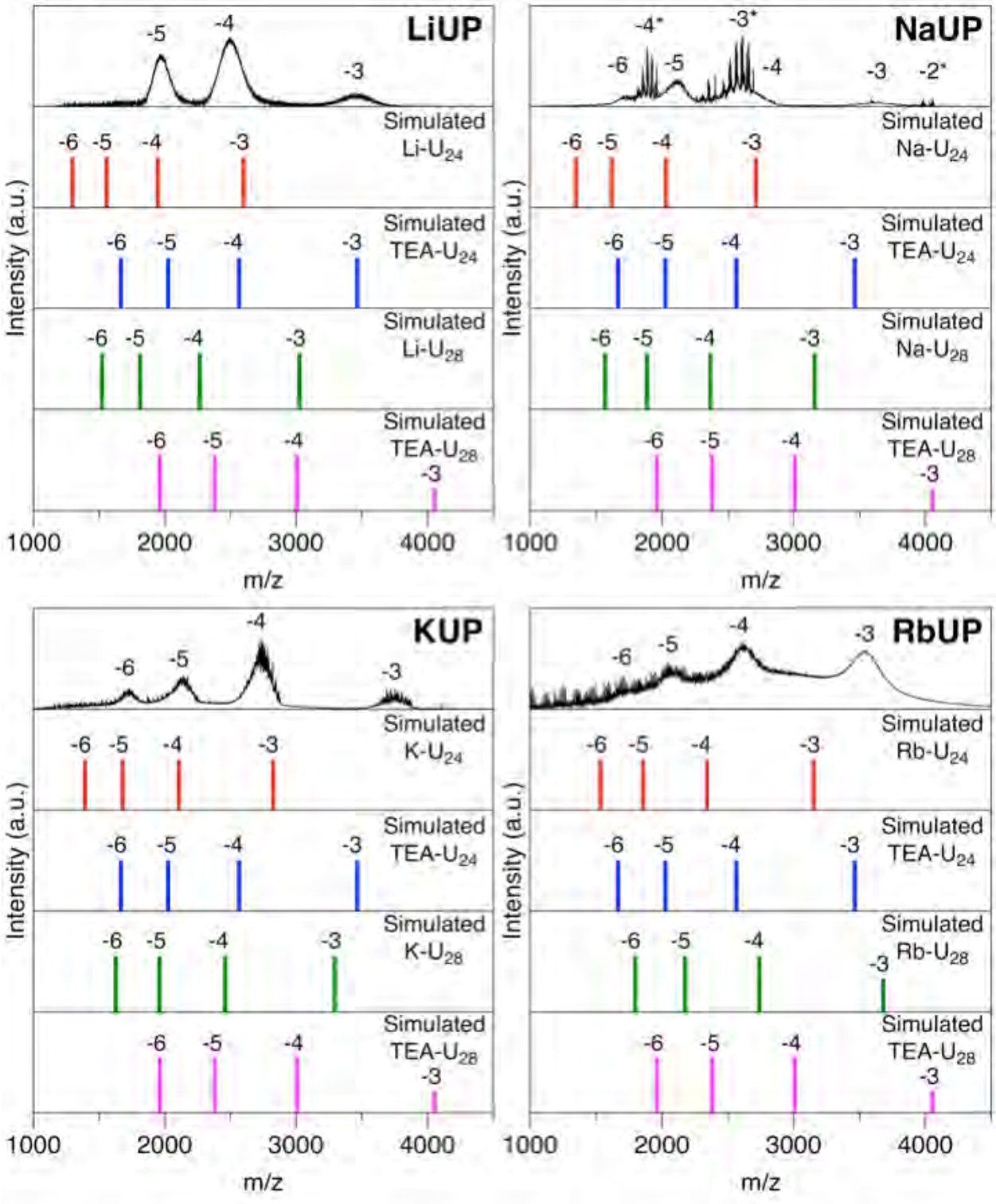

784

785

This is a preprint, the final version is subject to change, of the American Mineralogist (MSA)
Cite as Authors (Year) Title. American Mineralogist, in press.
DOI: https://doi.org/10.2138/am-2020-7106

Figure 10

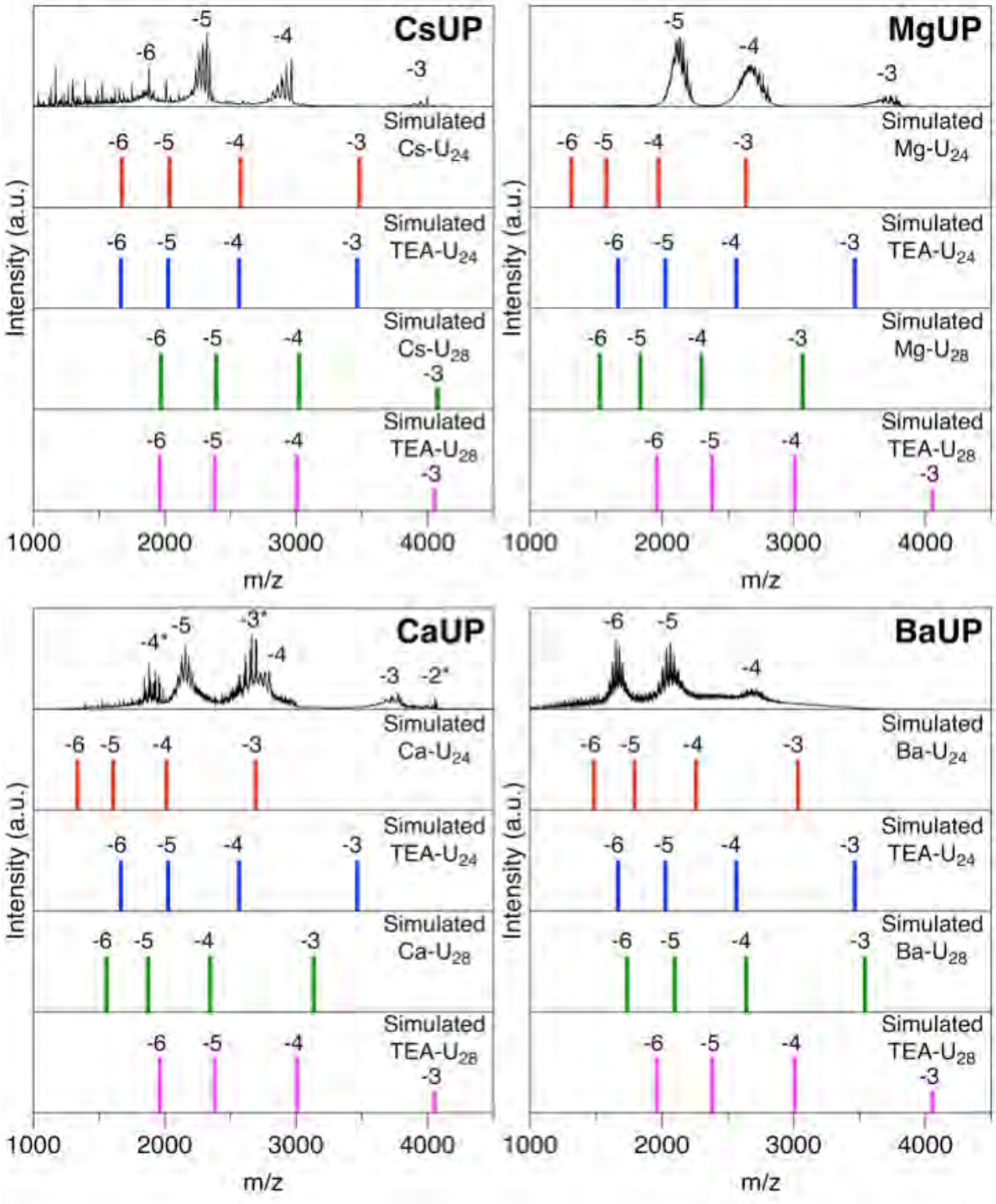

This is a preprint, the final version is subject to change, of the American Mineralogist (MSA)
Cite as Authors (Year) Title. American Mineralogist, in press.
DOI: https://doi.org/10.2138/am-2020-7106

Figure 11

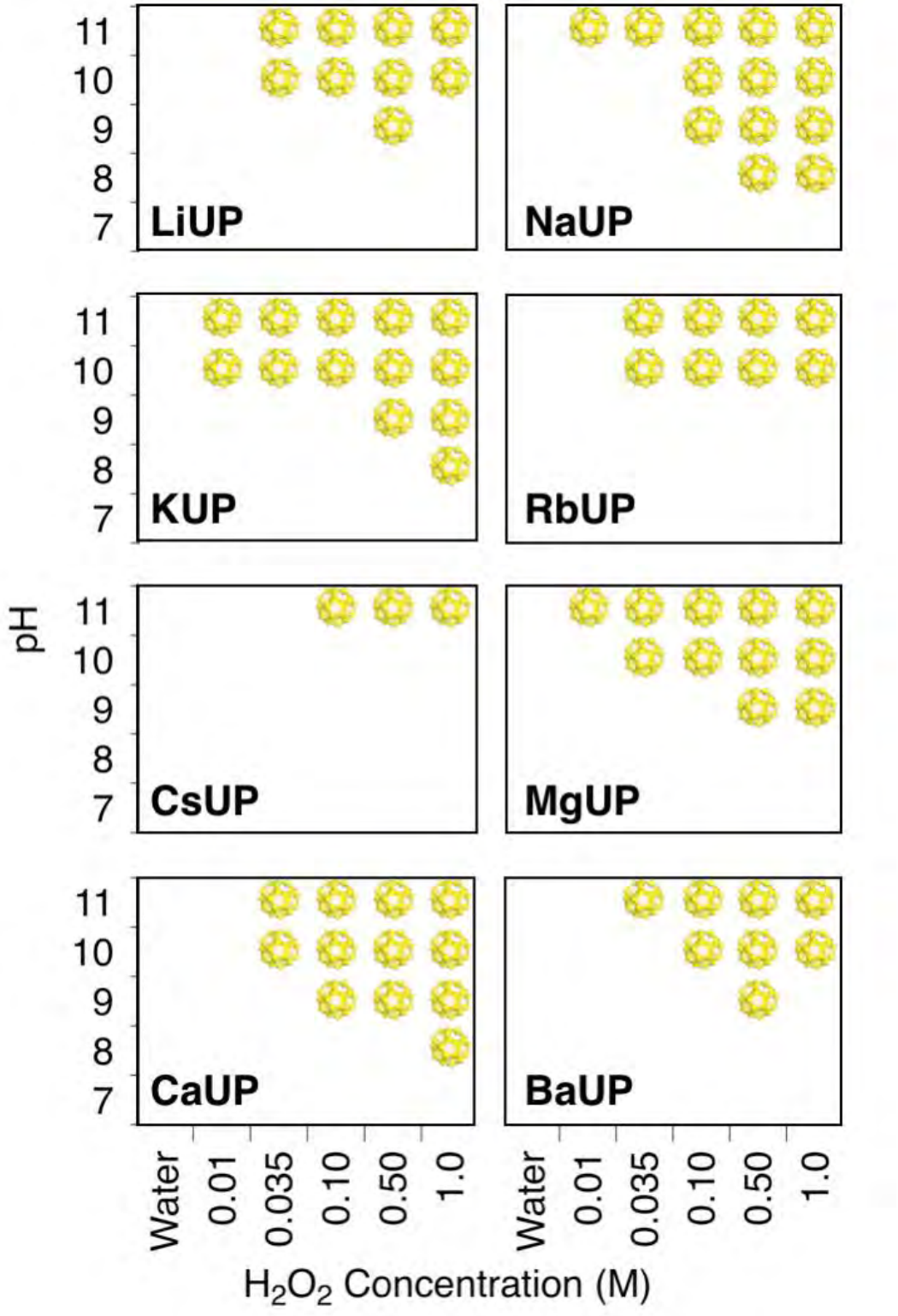

788

This is a preprint, the final version is subject to change, of the American Mineralogist (MSA)
Cite as Authors (Year) Title. American Mineralogist, in press.
DOI: https://doi.org/10.2138/am-2020-7106

Figure 12

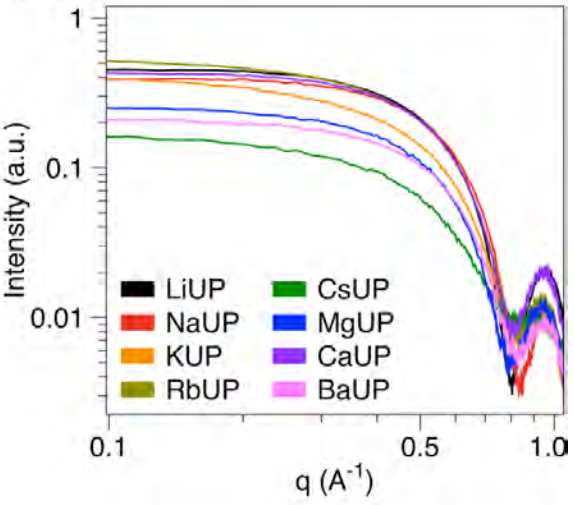

789

790

791